Multimodality Quantitative Assessments of Myocardial Perfusion Using Dynamic Contrast Enhanced Magnetic Resonance and ^{15}O-Labeled Water Positron Emission Tomography Imaging

G. Papanastasiou, M. C. Williams, M. R. Dweck, S. Mirsadraee, N. Weir, A. Fletcher, C. Lucatelli, D. Patel, E. J. R. van Beek, D. E. Newby, and S. I. K. Semple

***Abstract*—Kinetic modeling of myocardial perfusion imaging data allows the absolute quantification of myocardial blood flow (MBF) and can improve the diagnosis and clinical assessment of coronary artery disease (CAD). Positron emission tomography (PET) imaging is considered the reference standard technique for absolute quantification, whilst oxygen-15 (^{15}O)-water has been extensively implemented for MBF quantification. Dynamic contrast enhanced magnetic resonance imaging (DCE-MRI) has also been used for MBF quantification and showed comparable diagnostic performance against (^{15}O)-water PET studies. We investigated for the first time the diagnostic performance of two different PET MBF analysis softwares PMOD and Carimas, for obstructive CAD detection against invasive clinical standard methods in 20 patients with known or suspected CAD. Fermi and distributed parameter modeling-derived MBF quantification from DCE-MRI was also compared against (^{15}O)-water PET, in a subgroup of six patients. The sensitivity and specificity for PMOD was significantly superior for obstructive CAD detection in both per vessel (0.83, 0.90) and per patient (0.86, 0.75) analysis, against Carimas (0.75, 0.65) and (0.81, 0.70), respectively. We showed strong, significant correlations between MR and PET MBF quantifications ($r = 0.83 - 0.92$). However, DP and PMOD analysis demonstrated comparable and higher hemodynamic differences between obstructive versus (no, minor, or non)-obstructive CAD, against Fermi and Carimas analysis. Our MR method assessments against the optimum PET reference standard technique for perfusion analysis showed promising results in per segment level and can support further multimodality assessments in larger patient cohorts. Further MR against PET assessments may help to determine their comparative diagnostic performance for obstructive CAD detection.**

***Index Terms*—Coronary artery disease (CAD), dynamic contrast enhanced magnetic resonance imaging (DCE-MRI), kinetic modeling, Oxygen-15 (^{15}O)-water Positron emission tomography (PET).**

Manuscript received August 20, 2017; revised October 22, 2017 and December 11, 2017; accepted January 17, 2018. Date of publication January 23, 2018; date of current version May 2, 2018. The work of G. Papanastasiou was supported by the British Heart Foundation under Grant RE/08/001/23904. The work of M. C. Williams and M. R. Dweck was supported by the British Heart Foundation under Grant FS/11/014 and Grant CH/09/002. The work of E. J. R. van Beek was supported by the Scottish Imaging Network (www.sinapse.ac.uk). The work of D. E. Newby was supported in part by the British Heart Foundation under Grant FS/11/014 and Grant CH/09/002, and in part by the Wellcome Trust Senior Investigator Award under Grant WT103782AIA. *(Corresponding author: G. Papanastasiou.)*

G. Papanastasiou, M. C. Williams, M. R. Dweck, D. E. Newby, and S. I. K. Semple are with the Edinburgh Imaging Facility QMRI, University of Edinburgh, Edinburgh EH16 4TJ, U.K., and also with the Centre for Cardiovascular Science, University of Edinburgh, Edinburgh EH16 4TJ, U.K. (e-mail: g.papanas@ed.ac.uk; michelle.williams@ed.ac.uk; mdweck@exseed.ed.ac.uk; d.e.newby@ed.ac.uk; scott.semple@ed.ac.uk).

S. Mirsadraee was with the Edinburgh Imaging Facility QMRI, University of Edinburgh, Edinburgh EH16 4TJ, U.K. He is now with the Royal Brompton and Harefield Hospitals NHS Trust, London SW3 6NP, U.K. (e-mail: saeed.mirsadraee@ed.ac.uk).

N. Weir, A. Fletcher, C. Lucatelli, and E. J. R. van Beek are with the Edinburgh Imaging Facility QMRI, University of Edinburgh, Edinburgh EH16 4TJ, U.K. (e-mail: nick.weir@ed.ac.uk; alison.fletcher@ed.ac.uk; christophe.lucatelli@ed.ac.uk; edwin-vanbeek@ed.ac.uk).

D. Patel is with the Department of Radiology, Royal Infirmary of Edinburgh, Edinburgh EH16 4SA, U.K. (e-mail: dilip.patel@nhslothian.scot.nhs.uk).

This paper has supplementary downloadable material available at http://ieeexplore.ieee.org, provided by the author.

Color versions of one or more of the figures in this paper are available online at http://ieeexplore.ieee.org.

Digital Object Identifier 10.1109/TRPMS.2018.2796626

I. Introduction

MYOCARDIAL ischaemia is an essential prognostic determinant in coronary artery disease (CAD) and noninvasive methods for ischaemia assessment are important for the clinical management of patients with known or suspected CAD [1]. The current noninvasive clinical standard assessment for myocardial ischaemia is based on visual estimates from perfusion imaging data which are limited to identifying regional perfusion changes. The diagnostic performance of visual estimates is particularly compromised in conditions where MBF is diffusely abnormal, such as in multivessel disease, or where microvascular dysfunction may be present [2]. Kinetic modeling of myocardial perfusion imaging data can allow the absolute quantification of myocardial blood flow (MBF), which has the potential to improve the diagnosis of CAD, the assessment of coronary microcirculation and to precisely assess MBF changes following therapeutic interventions [2], [3].

Positron emission tomography (PET) imaging benefits from a direct relationship between signal intensity and the radioactivity concentration in the tissue of interest and is considered the reference standard technique for absolute quantification of

MBF [4]. In the context of MBF quantification, previous studies demonstrated the applicability of oxygen-15 (^{15}O)-water in PET perfusion imaging [4], [5]. For a metabolically inert freely diffusible tracer such as ^{15}O-water, single-tissue compartmental models are commonly used for MBF quantification without the need for radio-metabolite correction in the arterial blood [5], [6]. However, additional post-processing techniques are required to correct for spill-over effects between the left, right ventricular arterial blood, and myocardial tissue compartments and for the low-signal gradient between myocardial tissue and arterial blood [2], [4]–[6]. Perfusion analysis software implements different methods for spill-over correction and myocardial tissue delineation [4], [7], [8]. Although strong correlations in MBF quantification derived from different available PET perfusion analysis software (Carimas versus Cardiac VUer) have been previously shown [9], there is no previous work comparing the diagnostic ability of different perfusion analysis softwares to detect hemodynamic differences in the presence of obstructive CAD.

Dynamic contrast enhanced magnetic resonance imaging (DCE-MRI) using gadolinium-based extracellular contrast agents, has also been used to derive absolute quantification of MBF. Quantitative MR studies have previously shown comparable diagnostic performance for the detection of obstructive CAD [10]–[12] compared to quantitative ^{15}O-water PET [13]–[15]. Various MR models have been used to describe the kinetics of gadolinium-based contrast agents through the myocardium. Their diagnostic performance in detecting obstructive CAD has been assessed, with Fermi deconvolution modeling showing high diagnostic accuracy and being the most established approach [3], [10], [11]. The Fermi model is an empirical-mathematical model used to estimate MBF from MR perfusion data during first-pass of gadolinium-based extracellular contrast agents [10], [12]. Our group recently demonstrated that distributed parameter (DP) deconvolution modeling showed superior diagnostic performance against Fermi modeling for the detection of obstructive CAD using 3T MR and our results compared favorably against previous MR studies [12]. The DP model is based on tracer kinetics analysis and it can provide MBF quantification and additional information about coronary vascularity and permeability, such as estimates of intravascular space, extravascular-extracellular space, extraction fraction, permeability surface area product, and volume of distribution [12], [16], [17]. MR-derived MBF has been assessed against PET-derived MBF quantification in patients with CAD by using ammonia-13 (^{13}N) and rubidium-82 (^{82}Rb), which showed weak [18] and stronger [19] correlations, respectively. Despite these first multimodality MBF comparisons, Fermi- and DP modeling-derived MBF quantification from DCE-MR data have not been assessed against ^{15}O-water PET data in patients with CAD.

The objectives of this paper were twofold. We evaluated the diagnostic performance of two dedicated software packages, Carimas and PMOD, to detect obstructive CAD against the current clinical standard assessments of invasive coronary angiography and fractional flow reserve in a pilot population. We also assessed for the first-time Fermi- and DP modeling-derived MBF quantification from DCE-MRI against ^{15}O-water PET data, acquired in patients with CAD.

II. Methods

A. Study Population

The study was performed with the approval of the institutional research ethics committee and in accordance with the Declaration of Helsinki, as previously described [20]. Following informed consent, ^{15}O-water PET was acquired in 20 patients with history of stable angina and known or suspected CAD. Results are also presented here for a subset of six subjects who agreed to receive DCE-MRI, prior to standard clinical invasive CAD assessments (maximum interval between PET and MR imaging was seven days). All subjects were instructed to abstain from caffeine for 12 h before PET and MR imaging, which acts as an adenosine receptor antagonist and can otherwise affect adenosine-induced stress imaging [11], [14]. Exclusion criteria for subject recruitment included history of severely compromised renal function (serum creatinine greater than 2.26 mg/dL or glomerular filtration rate $\leq$ 30 mL/min), pregnancy and contraindications to adenosine or MR imaging. All patients underwent invasive coronary angiography and fractional flow reserve.

B. Cardiac Positron Emission Tomography

Rest and adenosine stress ^{15}O-water PET was performed using a hybrid PET-CT scanner (128-multidetector Biograph mCT, Siemens Medical Systems, Germany), as previously described [20]. Attenuation correction computed tomography imaging maps was acquired before rest and stress imaging. ^{15}O-water was produced by an on-site cyclotron (PETtrace 8, GE Healthcare, U.K.) and a radiowater generator (Hydex Oy, Finland) generated the ^{15}O-water bolus. For rest imaging, a target of 500 MBq ^{15}O-water bolus was injected intravenously over 15 s and the venous line was then flushed for another 2 min. The dynamic acquisition was performed over 5 min (14 frames $\times$ 5 s, 3 frames $\times$ 10 s, 3 frames $\times$ 20 s, and 4 frames $\times$ 30 s).

Following suitable radioactivity decay (of approximately 10 min), stress imaging was performed with intravenously administering adenosine for 4 min (140 μg/kg/min, Adenoscan, Sanofi Aventis) [13], [20]. The above protocol was then repeated using a further dose of 500 MBq ^{15}O-water bolus. Dynamic emission images were reconstructed using the standard UltraHD algorithm (Siemens Medical Systems, Germany) with a zoom of 2.00, matrix 128 $\times$ 128, voxels 3.18 $\times$ 3.18 $\times$ 3 mm.

C. Cardiac Magnetic Resonance Imaging

DCE-MRI imaging was acquired in a 3T Verio imaging system (Siemens, Healthcare Gmbh, Erlangen, Germany) using electrocardiogram-gating, as previously described [12]. Standard cardiac imaging planes and a short axis stack of left ventricular cine data were acquired using routine steady state free precession (TrueFISP) acquisitions. Modified look-locker inversion recovery (MOLLI) T_1 maps were acquired using

the Siemens Works in Progress Package #448, Quantitative Cardiac Parameter Mapping [21].

Stress imaging was performed by implementing the same adenosine infusion protocol as described above for 4 min [10], [12]. Fifty dynamic perfusion images were obtained at diastole across three short-axis view slices, covering 16 of the standard myocardial segments [22]. For dynamic imaging, a turbo-fast low angle shot (FLASH) saturation recovery prepared single-shot gradient echo pulse sequence was used with imaging parameters: flip angle 12°, repetition time/echo time 2.20 ms/1.07 ms, slice thickness 8 mm, preparation pulse delay to central line of *k*-space 100 ms, matrix size 192×108 and FoV 330 mm $\times$ 440 mm. Parallel imaging was performed with the application of GRAPPA (accelerator factor of 3) and partial Fourier acquisition of 0.75, which led to 48-phase encoding lines for each dynamic frame. An intravenous bolus of 0.05 mmol/kg of a gadolinium-based contrast agent (Gadovist, Bayer Healthcare) followed by 20 mL of 0.9% saline (Medrad Spectris Solaris, Medrad, USA) was injected at 4 mL/s using an MR compatible pump injector (Spectris Solaris, Medrad, Bayer). To allow clearance of residual contrast agent, rest perfusion imaging was performed 15 min after stress imaging, with the same acquisition protocol for all six subjects.

D. Invasive Coronary Angiography and Fractional Flow Reserve

Subjects underwent invasive coronary angiography and fractional flow reserve (clinical reference standard assessments) at the Royal Infirmary of Edinburgh. Invasive coronary angiography was performed via the radial artery as per standard clinical practice [20], [23]. Fractional flow reserve was assessed for major epicardial vessels and defined as the ratio between distal coronary pressure and aortic pressure measured simultaneously at maximal adenosine-induced (intravenous 140 μg/kg/min) hyperemia [23]. Obstructive CAD was defined as luminal stenosis $\geq$ 70% on invasive coronary angiography alone, or luminal stenosis $\geq$ 50% and fractional flow reserve $\leq$ 0.80 [12], [20]. (No, minor, or non)-obstructive CAD was defined as luminal stenosis $<$ 50% or luminal stenosis $\geq$ 50% and fractional flow reserve $>$ 0.80 [12], [20].

E. Quantitative ^{15}O-Water PET Analysis

^{15}O-water PET data were analyzed with two dedicated softwares (Carimas 2.9, www.turkupetcentre.net, Finland and PMOD 3.7, www.pmod.com, Switzerland), using single-tissue compartment modeling. The single-tissue compartment model can be mathematically described by

$$\frac{dC_t(t)}{dt} = \mathrm{MBF} \cdot C_a(t) - \frac{\mathrm{MBF}}{p} C_t(t) \tag{1}$$

where $C_t(t)$ and $C_a(t)$ are the radioactivity concentrations extracted by the myocardial tissue and the arterial blood from the left ventricular blood pool, respectively, and p is the partition coefficient of ^{15}O-water (i.e., myocardial to blood radioactivity concentration at equilibrium, when the net tracer flux between the compartments is zero; a constant value of 0.95 mL/mL for Carimas [7] and of 0.96 mL/mL for PMOD modeling [24] were used).

Myocardial contours were defined in short axis views, automatically with manual adjustment on digital subtraction images in Carimas [7], and semi-automatically with manual adjustment on images generated by factor analysis in PMOD [24]. In Carimas, digital subtraction images were automatically generated. For factor analysis in PMOD, volumes of interest were initially outlined within the left and right lungs, from which an average lung time activity curve was extracted. By time-shifting this lung time activity curve (automated time shift of -5 and 5 s for the right and left ventricle, respectively), approximations of two synthetic time activity curves in the right and left ventricle were derived. A third synthetic time activity curve corresponding to myocardial uptake was then calculated by solving the single-tissue compartment model with the shifted lung time activity curve (8 s) and by using a mean MBF value of 1 mL/min/mL [24]. All synthetic time activity curves were then used to automatically estimate weighted factors for the myocardium and left-ventricular blood pool for each dynamic frame, as described by Hermansen *et al.* [25] and factor analysis images were generated.

Carimas and PMOD performed correction for spill-over fractions from the left [7] and left and right ventricles [24], respectively. In Carimas post-processing, the measured radioactivity concentration derived from the images was expressed as a function of true radioactivity (radioactivity without the spill-over fractions) in the myocardium and left ventricular blood pool, as described in the following system of equations:

$$\begin{aligned} C_t(t) &= \mathrm{TF} \cdot C_{\mathrm{tt}}(t) + V_a \cdot C_{\mathrm{ta}}(t) \\ C_a(t) &= \beta \cdot C_{ta}(t) + (1-\beta) \cdot C_{\mathrm{tt}}(t) \end{aligned} \tag{2}$$

where TF, C_{tt}, V_a, C_{ta}, and β are the perfusable tissue fraction and true radioactivity in the myocardial tissue, the arterial vascular space (including the spill-over from the left ventricle blood pool), the true radioactivity in the left ventricular blood pool and the recovery coefficient (i.e., the ratio of measured to known radioactivity, a constant value of 0.93 was used), respectively. MBF quantification in Carimas was then performed in a 2-step process. Following substitutions in (1) and (2), and integration, the first operational equation was derived, which is a function of measured radioactivities in the left ventricular blood pool and myocardial tissue and fitted in a time activity curve extracted from the whole (nonsegmented) myocardium, using multilinear regression analysis for model fitting (see Table I) [26]. This first step allowed the calculation of the true radioactivity concentration in the left ventricular blood pool C_{ta}. By solving for $C_{\mathrm{tt}}(t)$ in the former expression of the system equation (2), integrating and substituting into equation (1), the final operational equation (second step) was then derived which was expressed as a function of true radioactivity $C_{\mathrm{ta}}(t)$ (measured from step 1) in the left ventricular blood pool (Table I). From the fitted parameters K_1', k_2', and V'_{fit} of this operational equation MBF, TF, and V_a were calculated and MBF parametric maps (per pixel

analysis) were generated. Mathematical derivations for true tissue radioactivity C_{tt}, true radioactivity in the left ventricular blood pool C_{ta} as well as for MBF, TF, and V_a calculations and explicit mathematical processing in Carimas, are further described in the Turku PET Centre Modeling report website link (www.turkupetcentre.net/reports/tpcmod0005.pdf).

In PMOD, by numerically integrating equation (1) and incorporating the spill-over corrections, the operational equation was derived (Table I) and fitted to the time activity curves extracted from myocardial tissue regions of interest using iterative nonlinear least square fitting (1-step process) [24]. In PMOD, the operational equation was expressed in terms of the fitted parameters TF, V_{LV}, V_{RV}, and $C_{a\mathrm{RV}}$: perfusable tissue fraction in the myocardial tissue, spill-over fraction from the left ventricle, spill-over fraction from the right ventricle, and radioactivity concentration in the right ventricle blood pool, respectively. Spill-over correction from the right ventricle (V_{RV}) was fitted for septal myocardial segments and was set to zero for nonseptal myocardial areas. Details about PMOD post-processing are further described in the PMOD website link (doc.pmod.com/PDF/PKIN.pdf). A list of notations for all kinetic modeling parameters are summarized in the supplementary material 1.

F. Quantitative DCE-MRI Analysis

Endocardial and epicardial MR contours were manually outlined using validated cardiac image analysis software (QMass, Medis, The Netherlands). Myocardial and arterial input function signal intensity-time curves were converted to gadolinium concentration-time curves using the method of Larsson *et al.* [27] as previously described [10], [12], [28]. According to this, the longitudinal relaxation rate R_1 $(1/T_1)$ changes linearly as a function of contrast agent concentration influx $C(t)$ in the tissue at time t, multiplied by its relaxivity r_1:

$$\Delta R_1 = C(t) \cdot r_1 \tag{3}$$

where $\Delta R_1 = R_1(t) - R_1(0) = (1/T_1(t)) - (1/T_1(0))$.

$T_1(0)$ is the native longitudinal relaxation rate and $T_1(t)$ is the longitudinal relaxation rate at time t of contrast enhancement. $R_1(t)$ can be calculated by adapting the MR signal equation for the saturation recovery prepared single-shot FLASH sequence [10], [28]

$$S(t) = \Psi \cdot f(R_1(t), PD, n) \tag{4}$$

where $S(t)$ is the equilibrium signal intensity at time t, Ψ is a calibration constant dependent on instrument conditions, such as the receiver gain, the proton density, and the flip angle α. PD is the prepulse delay which is the time between saturation pulse and the central line of k-space, n is the number of applied pulses of flip angle α. Ψ can initially be calculated from (4) using native $T_1(0)$ (measured with MOLLI [21]). $R_1(t)$ at time t of contrast enhancement can then be calculated from (4), using Ψ and $S(t)$ values extracted from the same region of interest. Contrast agent concentration-time curves can then be calculated using (3).

Model-dependent deconvolution analysis was implemented to measure MBF using Fermi and 1-barrier 2-region DP functions as previously described [12]. Fermi parameterization is an empirical 3-parameter model fit in which τ_o defines the width of the initial plateau of the tissue impulse response before it decays mono-exponentially at a rate given by the parameter k (see fitted parameters of Fermi function in Table I) [29]. The Fermi model is fitted to the first-pass phase of contrast enhancement. This is estimated by setting the end-point at the contrast agent concentration minimum in the arterial input function, before the recirculation component begins (this range varies from patient to patient and is commonly in the range between 20 and 35 dynamic frames) [12]. DP parameterization is a 4-parameter model fit based on tracer kinetics analysis and its tissue impulse response is expressed in terms of the fitted parameters T, T_c, and T_e : T is mean overall transit time, T_c is mean capillary transit time, and T_e is mean interstitial (i.e., extravascular-extracellular) transit time (Table I). DP modeling describes the intravascular space as a plug flow system, whilst assumes no axial indicator transport in the extravascular-extracellular space [16], [17]. The third and fourth fitted parameter for Fermi and DP deconvolution analysis, respectively, was MBF. DP model fitting was performed in the Laplace domain to avoid the discontinuities of the time step-function that can be present when fitting the DP model in the time domain [30]. To account for the time delay (between the onset of contrast enhancement in the blood pool and the myocardium), both models were fitted to the data multiple times from zero to six times the temporal resolution starting from the onset of contrast enhancement in the blood pool and the time delay reaching the optimal x^2 fit to the data was used in the analysis.

A standardized American Heart Association (AHA) 16-segment model of the heart was generated across all modeling applications [22]. In Carimas, the per pixel analysis was averaged for each of the 16-myocardial segments. For both ^{15}O-water PET and DCE-MR analysis, myocardial perfusion reserve (MPR) was also calculated by dividing the hyperemic by the resting MBF. MBF and MPR were quantified for each of the 16 myocardial segments and were then averaged per epicardial vessel territory (vessel territories corresponded to the three main coronary vessels, defined according to the 16 segment model [22]). Mean values for MBF at stress and MPR were classified accordingly in two groups for per vessel and per patient based analysis (see classification in the results section).

G. Statistical Analysis

Blinded and independent analysis of ^{15}O-water PET and DCE-MRI data was performed using dedicated statistics software (R Foundation for statistical computing, Vienna, Austria; MedCalc Software, Ostend, Belgium). Linear regression and Pearson's correlation coefficients were used to investigate correlations in MBF estimates between different modeling applications, for both ^{15}O-water PET and DCE-MRI, in a per segment and per vessel basis. Bland Altman analysis was implemented to investigate systematic bias between all modeling applications. Hemodynamic differences between obstructive versus (no, minor, or non)-obstructive CAD and

TABLE I

FITTED PARAMETERS AND OPERATIONAL EQUATIONS FOR CARIMAS (2-STEP PROCESSING), PMOD (^{15}O-WATER PET) ANALYSIS AND TISSUE IMPULSE RESPONSE FUNCTIONS FOR FERMI, 1-BARRIER 2-REGION DP (DCE-MRI) ANALYSIS ARE SHOWN. FITTED PARAMETERS FOR STEPS 1 AND 2 IN CAR: K_1, k_2, AND V_{fit} AND K_1', k_2', V_{fit}' FROM WHICH MBF, TF, AND V_a WERE CALCULATED, RESPECTIVELY. C_{CAR1} AND C_{CAR2} ARE THE OPERATIONAL EQUATIONS (1) AND (2) FOR CARIMAS PROCESSING, RESPECTIVELY. FITTED PARAMETERS FOR PMOD: MBF, TF, V_{LV}, AND V_{RV}. FITTED PARAMETERS FOR FERMI: MBF, τ_0 CHARACTERIZED THE WIDTH OF THE SHOULDER OF THE FERMI FUNCTION AND k DETERMINED THE DECAY RATE OF THE TISSUE IMPULSE RESPONSE $R(t)$ DUE TO CONTRAST AGENT WASH-OUT, t IS THE TIME VARIABLE. FITTED PARAMETERS FOR DISTRIBUTED PARAMETER: MBF, T IS MEAN OVERALL TRANSIT TIME, Tc IS MEAN CAPILLARY TRANSIT TIME, Te IS MEAN INTERSTITIAL (I.E., EXTRAVASCULAR-EXTRACELLULAR) TRANSIT TIME. CAR: CARIMAS, C_t: THE IMAGE-DERIVED RADIOACTIVITY CONCENTRATION IN THE MYOCARDIAL TISSUE, C_{ta}: THE TRUE (WITHOUT SPILL-OVER FRACTION FROM THE MYOCARDIAL TISSUE) RADIOACTIVITY CONCENTRATION IN THE LEFT VENTRICLE, MBF: MYOCARDIAL BLOOD FLOW, TF: PERFUSABLE TISSUE FRACTION IN THE MYOCARDIAL TISSUE, V_{LV}: SPILL-OVER FRACTION FROM THE LEFT VENTRICLE, V_{RV}: SPILL-OVER FRACTION FROM THE RIGHT VENTRICLE, DP: DISTRIBUTED PARAMETER MODEL. $s = i \cdot 2 \cdot \pi \cdot f$ WHERE f IS THE FREQUENCY VARIABLE IN THE FOURIER TRANSFORMED DATA

Model/^{15}O-water PET	**Fitted parameters**	**Operational equation**
CAR	K_1, k_2, V_{fit}	$C_{CAR1}(t) = K_1 \cdot \int_0^t C_a(t)dt - k_2 \cdot \int_0^t C_t(t)dt + V_{fit} \cdot C_a(t)$ (1)
	K_1', k_2', V_{fit}'	$C_{CAR2}(t) = K_1' \cdot \int_0^t C_{ta}(t)dt - k_2' \cdot \int_0^t C_t(t)dt + V_{fit}' \cdot C_{ta}(t)$ (2)
PMOD	MBF, TF, V_{LV}, V_{RV}	$C_{PMOD}(t) = TF \cdot \left(MBF \cdot \int_0^t C_a(t)dt - \frac{MBF}{p} \cdot \int_0^t C_t(t)dt \right) + V_{LV} \cdot C_a(t) + V_{RV} \cdot C_{aRV}(t)$
Model/DCE-MRI	**Tissue impulse response (*R*)**	
Fermi	MBF, τ_0, k	$R(t) = \frac{1}{\exp\left[(t-\tau_o)\cdot k\right]+1}$
DP	MBF, T, T_c, T_e	$R(s) = \frac{1-\exp\left[-s\cdot\left(T + s\cdot T_c\cdot T_e\right)/\left(1+s\cdot T_e\right)\right]}{s}$

between all modeling applications in a per segment basis, were investigated by implementing two sample t-test (two-sided P value < 0.05 were considered significant). For the Carimas versus PMOD comparison, receiver-operating characteristic (ROC) analysis was used on a per vessel and per patient basis to determine threshold values for absolute MBF at stress and MPR with the greatest sensitivity and specificity to detect obstructive versus (no, minor, or non)-obstructive CAD (group 2 versus group 1, see results). The area under the curve (AUC) was calculated using trapezoidal numerical integration and a DeLong *et al.* [31] nonparametric comparison was performed to compare the diagnostic performance of ^{15}O-water PET quantitative methods. The maximal Youden Index was used to determine the optimal threshold values [10], [12].

III. RESULTS

The baseline characteristics of the full patient cohort are presented in Table II. Quantitative ^{15}O-water PET analysis was performed in 20 patients, in which the diagnostic performance of Carimas versus PMOD in detecting obstructive CAD was investigated. For six of these patients, quantitative DCE-MRI analysis was also performed and correlations and agreements in MBF measurements were investigated against ^{15}O-water PET (Fig. 1).

For each subject, MBF quantification across all four modeling methods was performed for each of the 16 myocardial segments, in per segment analysis. Myocardial segments with (no, minor, or non)-obstructive and obstructive CAD were then classified based on the invasive coronary angiography and fractional flow reserve data, in groups 1 and 2, respectively. In

TABLE II

PATIENT CHARACTERISTICS ($N = 20$) PRESENTED

Baseline characteristics	
Age (years)	62 ± 5
Male/Female	15/5
Body mass index (kg/m^2)	29 ± 5
Hypertension	18
Hypercholesterolemia	18
Diabetes mellitus	3
Cerebrovascular disease	2
Current smoker	2
Ex-smoker (>1 month)	9
Family history	9
Previous revascularisation	6
Invasive methods (per vessel)	
Group 1	13
Group 2	7

per vessel analysis, segmental MBF values were averaged per epicardial vessel territory (three main coronary vessels, as per the 16-segment AHA model) [10], [15], [22]. Vessel territories with (no, minor, or non)-obstructive CAD were classified in group 1 and vessels with obstructive CAD were classified in group 2. For per patient analysis, patients with all vessel territories detected with (no, minor, or non)-obstructive CAD were classified in group 1, whilst patients with at least one vessel identified with obstructive CAD, were classified in group 2 [12].

A. Carimas Versus PMOD Analysis

Quantitative ^{15}O-water PET analysis was performed in 60 vessel territories in total (20 patients, 3 vessel territories

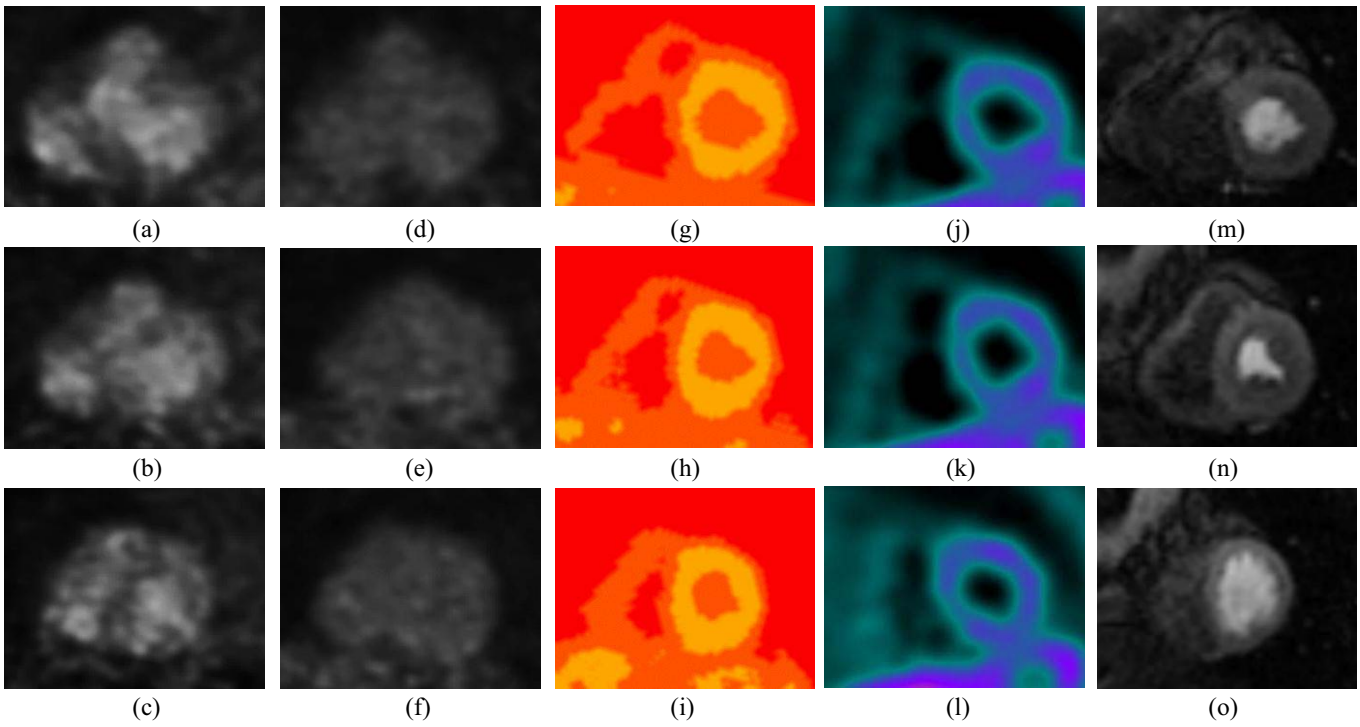

Fig. 1. Perfusion images showing myocardial ^{15}O-water PET radioactivity in unprocessed data at the (a)–(c) peak of contrast enhancement and (d)–(f) during the wash-out phase, from a patient with nonobstructive CAD. Note that the low signal gradient between the myocardial tissue and arterial blood. (g)–(i) Carimas and (j)–(l) PMOD post-processed images are shown, generated using digital subtraction and factor analysis, respectively, for the same patient data (note that the two softwares use different color bars to show radioactivity in the images). The entire myocardial wall is well delineated in both Carimas and PMOD. (m)–(o) DCE-MR images showing peak contrast enhancement in the myocardium from the same patient. (a), (d), (g), (j), and (m) Basal, (b), (e), (h), (k), and (n) mid-ventricular, and (c), (f), (i), (l), and (o) apical slices are illustrated.

each). Seven patients had at least one vessel identified with obstructive CAD: 3 patients had 1-vessel disease, 3 had 2-vessel disease, and 1 had 3-vessel disease. Examples of model fitting and arterial input functions from both modeling approaches are presented in Fig. 2.

On linear regression and Pearson's correlation, PMOD and Carimas-derived MBF showed strong, significant correlations ($P < 0.001$), in both per segment ($r = 0.88$) and per vessel ($r = 0.91$) analysis. Carimas overestimated PMOD MBF estimates at stress ($P < 0.05$), whilst underestimated PMOD MBF estimates at rest ($P < 0.01$).

On Bland Altman analysis, the average bias was calculated as the Carimas-derived estimates minus the PMOD modeling-derived estimates. The systematic bias was low in both per segment and per vessel basis: 0.16 (−1.18, 1.50) versus 0.16 (−0.95, 1.28), respectively.

Hemodynamic differences between obstructive versus (no, minor, or non)-obstructive CAD were initially assessed in a per segment basis. Significant differences in stress MBF values between myocardial segments classified in group 1 versus group 2 were higher (4 orders of magnitude) for PMOD modeling against Carimas modeling, respectively ($P < 0.0001$).

ROC analysis curves were subsequently investigated in per vessel and per patient analysis, shown in Fig. 3. Mean (SD) values for Carimas and PMOD-derived MBF and MPR in groups 1 and 2 for per vessel analysis are shown in Table III. All hemodynamic thresholds estimated on ROC analysis are presented in Table IV. In per vessel ROC analysis, the AUCs for PMOD were significantly higher compared to Carimas modeling, for both MBF at stress and MPR (Table IV). The diagnostic performance of PMOD consistently outperformed Carimas modeling (Table IV).

Mean (SD) values for Carimas and PMOD-derived MBF and MPR in groups 1 and 2 for per patient analysis are presented in Table III. In per patient ROC analysis, the AUCs for PMOD were significantly higher whilst the diagnostic performance was consistently superior for PMOD modeling compared to Carimas modeling, for both MBF at stress and MPR (Table IV).

B. DCE-MRI Versus ^{15}O-Water PET

Quantitative ^{15}O-water PET against DCE-MRI analysis was performed in 18 vessel territories in total (six patients, three vessel territories each). Mean values (SD) and significant differences for all modeling applications, for groups 1 and 2, are shown in Fig. 4. Significant differences between groups 1 and 2 were equivalent (P values in the same order of magnitude) for DP against PMOD modeling (Fig. 4, $P < 0.0001$). Significant differences were higher (two orders of magnitude) for DP and PMOD modeling against Carimas and Fermi modeling, respectively (Fig. 4, $P < 0.0001$). An example file presenting per segment analysis across all models for a patient with obstructive CAD is shown in the supplementary material 2.

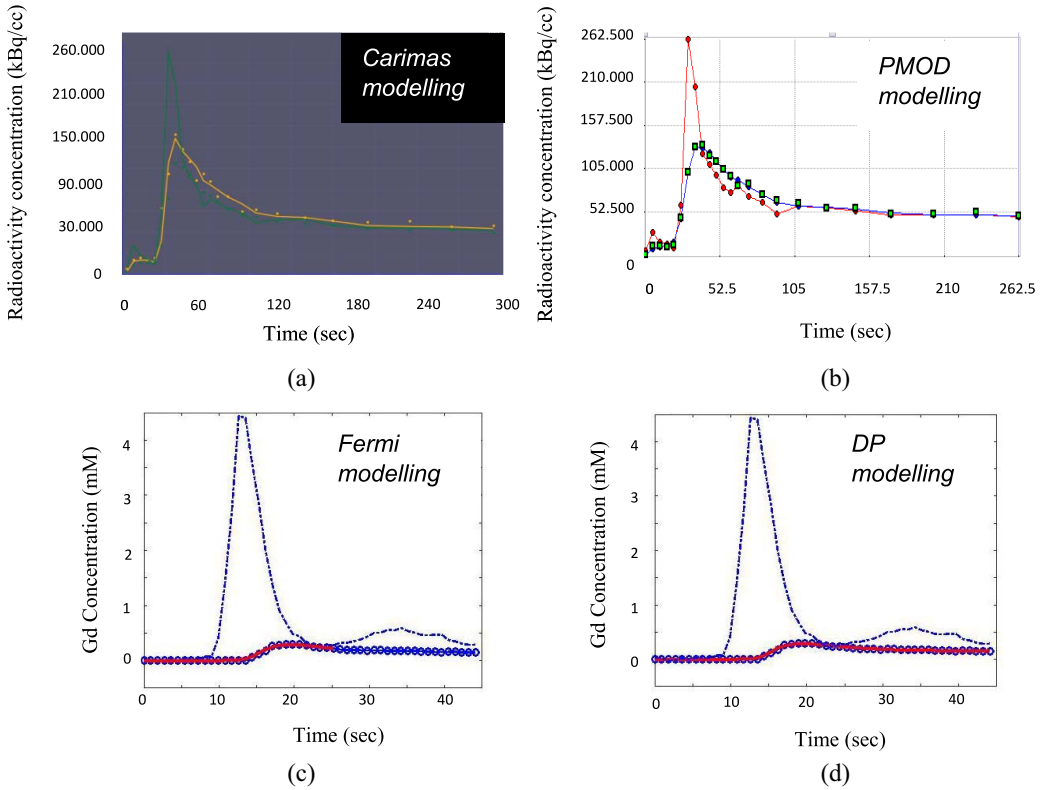

Fig. 2. Perfusion curves and model fits extracted for all modeling applications from the AHA-myocardial segment 8 of the same patient with nonobstructive CAD in (a) and (b) PET and (c) and (d) MR. The green, dotted, and solid yellow curves are the arterial input function, myocardial tissue time activity curve, and model fit in (a) Carimas, the red, squared green, and blue curves are the arterial input function, myocardial tissue time activity curve, and model fit in (b) PMOD, respectively, for the same myocardial segment. The dashed-dotted, dotted-solid blue, and red curves are the arterial input function, myocardial tissue Gd concentration-time curve, and models fits for (c) Fermi and (d) DP modeling, respectively, from the same MR myocardial segment.

TABLE III
MEAN (SD) VALUES IN PER VESSEL AND PER PATIENT CLASSIFICATION FOR CARIMAS (CAR) AND PMOD MODELING

Mean (SD) MBF (mL/min/mL), MPR	**Per vessel**				**Per patient**			
	CAR		**PMOD**		**CAR**		**PMOD**	
	G1	**G2**	**G1**	**G2**	**G1**	**G2**	**G1**	**G2**
MBF at stress	3.21 (1.03)	2.15 (1.10)	2.83 (0.98)	1.60 (0.67)	3.38 (0.74)	2.34 (0.87)	3.06 (0.74)	1.74 (0.74)
MBF at rest	0.81 (0.17)	0.82 (0.14)	0.87 (0.16)	0.89 (0.18)	0.78 (0.16)	0.77 (0.16)	0.86 (0.14)	0.88 (0.17)
MPR	4.13 (1.74)	2.87 (2.22)	3.35 (1.25)	1.89 (1.27)	4.20 (1.15)	3.27 (1.33)	3.55 (0.91)	2.12 (0.97)

There were no significant differences between DP, Carimas, and PMOD modeling-derived MBF values at stress. Fermi modeling significantly overestimated MBF compared with all other modeling applications, both at stress and rest ($P < 0.01$). DP and Fermi modeling-derived values overestimated Carimas and PMOD modeling-derived values at rest ($P < 0.001$).

On linear regression and Pearson's correlation analysis, MBF estimates derived from ^{15}O-water PET and DCE-MRI data, were initially separately assessed. Carimas versus PMOD MBF values, as well as DP versus Fermi MBF values, showed significant correlations in per segment and per vessel analysis (Table V, $P < 0.001$).

On Bland Altman analysis, the average bias was calculated as the Carimas-derived estimates minus the PMOD modeling-derived estimates for ^{15}O-water PET data; and Fermi modeling-derived estimates minus the DP modeling-derived estimates for DCE-MRI data (Table V). The systematic bias was low, mainly for ^{15}O-water PET data, which was eliminated in per vessel analysis.

Subsequently, MBF measurements from DP and Fermi modeling from DCE-MRI data were compared against measurements from Carimas and PMOD modeling from ^{15}O-water PET data. Similarly, there were significant ($P < 0.001$) correlations for all comparisons, whilst DP and Fermi modeling showed consistently better correlations with PMOD modeling (Fig. 5), compared to Carimas analysis (Table V).

On Bland Altman analysis, the average bias was calculated as PMOD- and Carimas modeling-derived estimates minus DP modeling-derived estimates; and the Fermi modeling-derived estimates minus the PMOD- and Carimas-modeling-derived estimates (Table V). The lowest systematic bias was observed between PMOD and DP-modeling derived MBF, although with broader limits of agreement, compared to Fermi modeling (Table V, Fig. 5).

TABLE IV
AUCs, Diagnostic Performance, Hemodynamic Thresholds and AUC Differences Between Methods on ROC Analysis, Are Presented. CAR, MBF, and MPR (Significant Differences Are Indicated With *). Values Inside Parentheses Show SD

Statistical analysis/ Model	Per vessel		Per patient	
	CAR	PMOD	CAR	PMOD
AUCs from ROC analysis				
MBF at stress	0.73 (0.62, 0.84)	0.87 (0.79, 0.95)	0.78 (0.68, 0.88)	0.90 (0.84, 0.96)
MPR	0.70 (0.60, 0.80)	0.85 (0.77, 0.93)	0.67 (0.55, 0.79)	0.86 (0.76, 0.96)
Diagnostic performance				
Sensitivity-MBF at stress	0.75 (0.56, 0.94)	0.83 (0.70, 0.96)	0.81 (0.62, 1.00)	0.86 (0.73, 0.99)
Specificity-MBF at stress	0.65 (0.52, 0.78)	0.90 (0.81, 0.99)	0.70 (0.55, 0.85)	0.75 (0.61, 0.89)
Sensitivity-MPR	0.67 (0.43, 0.90)	0.75 (0.50, 1.00)	0.57 (0.36, 0.78)	0.67 (0.49, 0.85)
Specificity-MPR	0.73 (0.61, 0.85)	0.85 (0.73, 0.97)	0.77 (0.61, 0.92)	0.95 (0.91, 0.99)
Thresholds on ROC analysis				
MBF at stress (mL/min/mL)	2.45	2.00	2.50	2.50
MPR	3.05	2.40	3.05	2.40
Difference in AUC of ROC curves between CAR and PMOD				
MBF at stress	0.14 (0.00, 0.28) *		0.12 (0.01, 0.22) *	
MPR	0.15 (0.00, 0.30) *		0.19 (0.07, 0.32) *	

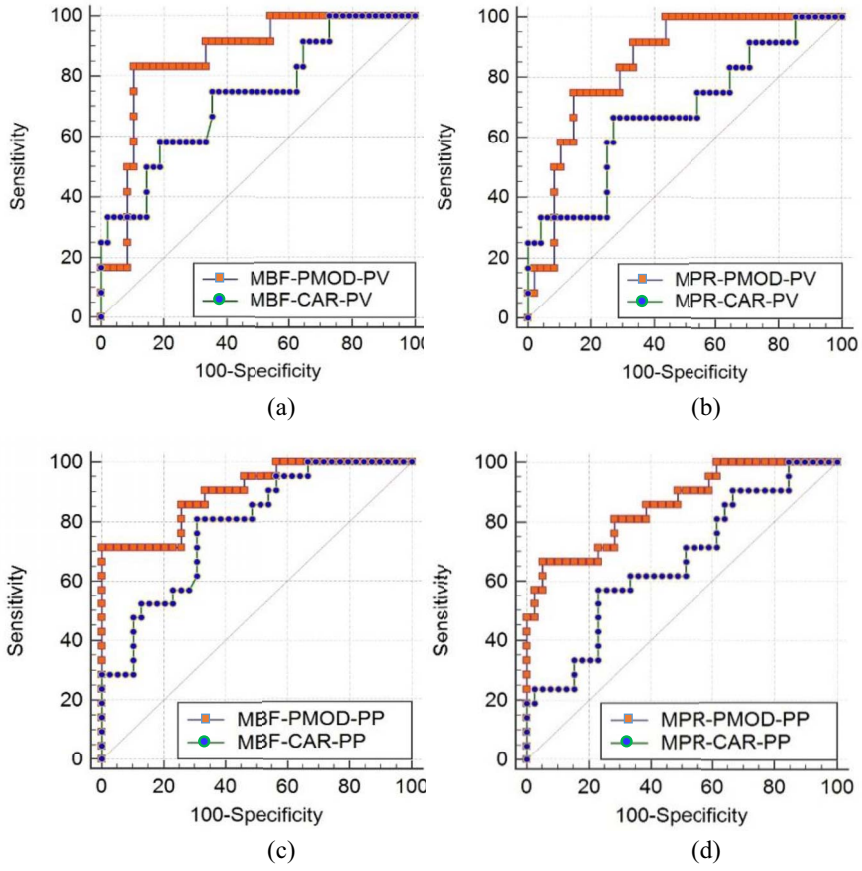

Fig. 3. ROC curves demonstrating diagnostic performance for both Carimas and PMOD modeling in (a) and (b) per vessel and (c) and (d) per patient analysis showing measures of (a) and (c) MBF at stress, and (b) and (d) MPR.

IV. Discussion

The main outcomes of this paper demonstrated that PMOD showed higher hemodynamic differences between obstructive versus (no, minor, or non)-obstructive CAD in per segment-based analysis, as well as consistently outperforming Carimas modeling in both per vessel and per patient analysis. Beyond strong, significant correlations across all MR versus PET comparisons, DP and PMOD analysis showed comparable and higher hemodynamic differences between obstructive versus (no, minor, or non)-obstructive CAD, against Fermi and Carimas analysis.

A. Carimas Versus PMOD

To date, this is the first study assessing diagnostic performance for the detection of obstructive CAD, using

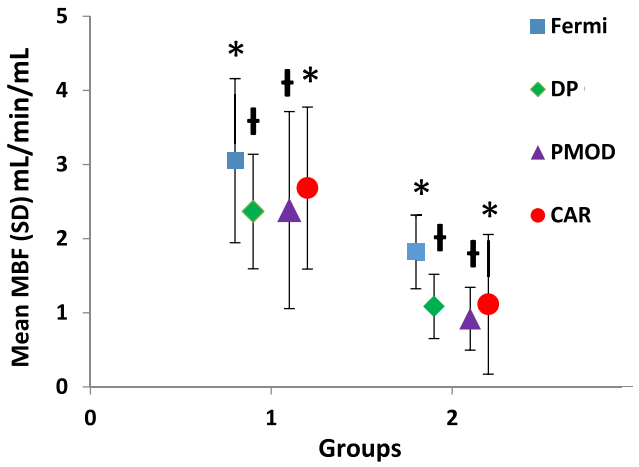

Fig. 4. Mean MBF (SD) and significant differences between groups 1 (nonobstructive CAD) and 2 (obstructive CAD), for all modeling applications. All models showed significant differences between groups 1 and 2 ($P < 0.0001$). Significant differences were higher for PMOD and DP modeling, compared to CAR and Fermi modeling († show two orders of magnitude smaller P values compared to *).

more than one perfusion analysis software. Our correlation coefficients for Carimas versus PMOD estimates are in agreement with similar comparisons performed in ^{15}O-water PET [4] and in ^{82}Rb-rubidium PET [32], which showed good correlations between different cardiac PET perfusion quantification software. Despite the larger patient cohorts previously analyzed, none of these studies compared the diagnostic ability of the different software examined in detecting reduced blood flow in the presence of obstructive CAD. In our pilot cohort, we assessed hemodynamic differences between obstructive versus (no, minor, or non)-obstructive CAD in per segment analysis, as well as performed full diagnostic performance in per vessel and per patient level on ROC analysis. We demonstrated that PMOD consistently showed higher hemodynamic differences and superior diagnostic performance in detecting obstructive CAD, compared with Carimas. These results indicate that it may be important to fully assess hemodynamic differences and diagnostic performance, beyond just MBF cross-correlations, when different perfusion softwares are compared.

The diagnostic performance for PMOD was in agreement with a previous ^{15}O-water PET study [14], whilst compared favorably against other findings on a per vessel [33], or per patient basis [8]. The highest diagnostic performance for the detection of obstructive CAD was reached by PMOD-derived MBF at stress in per vessel analysis, which is consistent with a previous ^{15}O-water study where the PMOD-derived sensitivity and specificity were higher in per vessel compared to per patient-based analysis [33]. Moreover, the diagnostic performance of MBF at stress was consistently higher compared to MPR for both Carimas and PMOD, as previously demonstrated [8], [15], [33]. In this paper, a small pilot cohort was investigated with a low number of patients with obstructive and multivessel CAD. Microvascular dysfunction that may be present in patients with minor or nonobstructive CAD (see risk factors in Table II: rates for hypertension, hypercholesterolemia, ex-smokers, and revascularization [12], [14]), can also lead to MBF reductions, which in turn can compromise the specificity for the detection of obstructive CAD-specific MBF reductions [12]. We showed that Carimas overestimated PMOD estimates at stress hence, any MBF overestimations in myocardial segments classified with obstructive CAD could explain its lower sensitivity versus PMOD, in our data. These factors together with differences in patient cohorts and acquisition protocols can explain the lower diagnostic performance detected for the case of Carimas modeling, in comparison with a previous study which used the same software in a larger patient cohort (38 out of 104 patients scanned had obstructive CAD) and higher ^{15}O-water doses (maximum of 1100 MBq for each ^{15}O-water injection) [13].

Our hemodynamic thresholds on ROC analysis for PMOD and Carimas-derived MBF (Table V) were consistent with previous ^{15}O-water PET studies which identified thresholds in the range between 1.85 and 2.50 mL/min/mL, for both per vessel and per patient-based analyses [8], [13], [14], [33], [34]. Furthermore, these thresholds agree with Fermi (2.49, 2.60 mL/min/mL) and DP (1.75, 2.00 mL/min/mL) modeling-derived thresholds in per vessel and per patient analysis, respectively, estimated by our group [12]. Differences in ^{15}O-water doses, PET protocols and scanners, image reconstruction, post-processing techniques, and angiographic thresholds defining obstructive CAD can explain any hemodynamic threshold variations between ^{15}O-water PET studies, including the current work [13], [33]. We also demonstrated that Carimas overestimated and underestimated PMOD estimates at stress and rest, respectively, which can explain the higher threshold values identified for Carimas-derived MPRs, in both per vessel and per patient analysis.

Technical disparities between Carimas and PMOD can interpret the diagnostic performance differences demonstrated. Although no spill-over correction from the right ventricle in Carimas means that it would mainly affect MBF measurements in septal myocardial segments (anatomically located between the left and right ventricle), it also overestimated PMOD MBF values at stress in nonseptal areas. A considerable disparity between Carimas and PMOD post-processing, is the pixel by pixel-based (using a linear least square approach described in [26]) versus segment-based (using standard nonlinear least square fitting) method for model fitting, respectively. Differences between linear versus nonlinear least square approaches have been assessed using single-tissue compartmental modeling and demonstrated that linear least square methods may compromise the accuracy of MBF quantification [26], [35]. In contrast, other studies showed that the linear least square and/or generalized linear least square (designed to reduce estimation bias of the linear least square method) approaches can provide accurate estimates of blood flow, compared to the standard nonlinear least square (segment-based) method [36]–[38]. Boellaard *et al.* [39] compared different methods for pixel-based MBF analysis and demonstrated that the basis function method was independent of the noise level and provided the most accurate perfusion

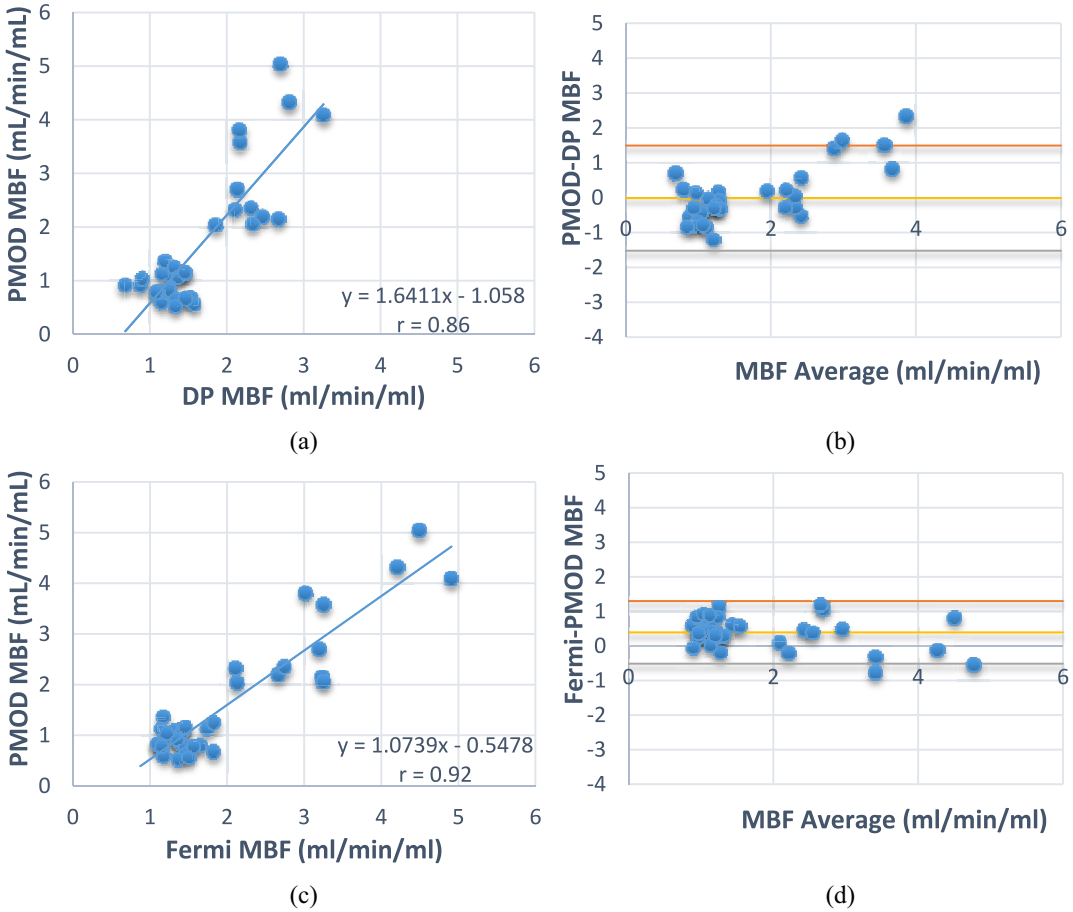

Fig. 5. (a) and (c) Linear regression, Pearson's correlation (r) and (b) and (d) Bland Altman plot analysis (values coordinated accordingly to allow positive average bias) for DP and Fermi versus PMOD modeling-derived MBF, in per vessel analysis.

TABLE V
PEARSON'S COEFFICIENTS AND BLAND ALTMAN ANALYSIS FOR ALL MULTIMODALITY COMPARISONS ARE PRESENTED. CAR, DP MODEL, MBF, PS: PER SEGMENT, AND PV: PER VESSEL

Statistical analysis/Model	Pearson's r (MBF-PS)	Pearson's r (MBF-PV)	Bland Altman (MBF-PS)	Bland Altman (MBF-PV)
CAR vs PMOD	0.91	0.96	0.14 (-1.24, 1.53)	0.00 (-0.70, 0.70)
PMOD vs DP	0.79	0.86	0.03 (-1.57, 1.63)	-0.01 (-1.52, 1.49)
CAR vs DP	0.73	0.83	0.16 (-1.61, 1.93)	0.13 (-1.40, 1.66)
Fermi vs PMOD	0.84	0.92	0.39 (-0.86, 1.64)	0.39 (-0.51, 1.30)
Fermi vs CAR	0.76	0.86	0.24 (-0.46, 1.94)	0.25 (-0.95, 1.45)
Fermi vs DP	0.86	0.94	0.39 (-0.86, 1.64)	0.36 (0.63, 1.34)

estimates, compared to the linear least square and generalized linear least square approaches. Further work is needed to elucidate to what degree the linear least square approach used has affected the diagnostic performance of the Carimas software. Another important difference in the post-processing between Carimas and PMOD is the 2-step versus 1-step mathematical modeling, respectively. This involves fitting different operational equations for the two softwares and thus, MBF estimations differ: MBF is indirectly estimated through the fitted parameter K_1' in Carimas (described in methods, Table I, and Carimas documentation), whilst directly calculated from the fitted parameter MBF in PMOD. These disparities can suggest that any Carimas-derived MBF overestimations may be due to a combination of the above technical differences, beyond just methodological differences in the spill-over correction approach.

B. DCE-MR Versus ^{15}O-Water PET

We demonstrated for the first time strong correlations between DP/Fermi modeling- (from DCE-MRI) versus Carimas/PMOD modeling-derived values (from ^{15}O-water PET) in a subgroup of patients with CAD. This is also the first study comparing DP modeling against PET. In per segment-based analysis, we showed that hemodynamic differences between obstructive versus (no, minor, or non)-obstructive CAD were comparable for DP and PMOD, against Fermi and Carimas analysis. Due to the small number of subjects

in this subgroup of patients, it was not possible to perform a full diagnostic performance comparison (ROC analysis) for obstructive CAD detection across all our MR versus PET comparisons. However, our PET findings are consistent with the higher hemodynamic differences presented in our full cohort for PMOD in per segment level, for which superior diagnostic performances were consistently demonstrated against Carimas. Similarly, our MR findings are also consistent with the higher hemodynamic differences showed in our previous study for DP modeling in per segment level [12], for which higher diagnostic performances were consistently shown, against Fermi modeling.

Direct comparisons in correlation coefficients against previous MR versus PET studies are difficult because of variations in the image acquisition and analysis techniques [18], [19], [40]–[42]. However, our correlation coefficients compare favorably against previous studies comparing two-compartmental and Fermi MR-derived MBF against PET [19], [40] respectively, whilst are in agreement with other studies that assessed model-independent, model-independent/Fermi, and single-tissue compartment/Patlak MR derived MBF against PET [18], [41], [42], respectively. Two studies have previously compared DCE-MRI against ^{15}O-water PET data in healthy subjects [40], [42]. Pärkkä *et al.* [40] used 18 healthy volunteers and showed weaker perfusion correlations compared to our data analysis. Despite the larger healthy volunteer cohort used in this paper, it was not possible to investigate correlations across different hemodynamic states (MBF at stress in no, minor, non-obstructive, obstructive CAD, MBF at rest), assessed in our pilot cohort. Also for the MR analysis, the parameter K^{trans} was estimated from which a direct estimate of MBF is not possible, as its physiological interpretation reflects a mixture of blood flow and the permeability surface area product [17]. Our correlation coefficients agree with the study by Tomiyama *et al.* [42], which showed strong correlations between single-tissue compartment model (per vessel analysis across 10 subjects, $r = 0.92$) and Patlak model (per vessel analysis across ten subjects, $r = 0.80$) derived MBF against an in-house software for ^{15}O-water PET data analysis.

Although PET imaging is considered the reference standard for MBF quantification and therefore it is important for validating MR perfusion, each tracer has its own limitations [2], [5], [6]. The main limitations for the analysis of ^{15}O-water are the need to correct for the high ^{15}O-water activity in the blood pool and for the spill-over from the left and right ventricles [2], [5]. Our multimodal comparisons against invasive methods showed that PMOD may be able to effectively minimize the impact of the above limitations for MBF quantification compared to Carimas, and that it may be a useful analysis tool for validating quantitative MR perfusion.

DP modeling did not show significant differences against Carimas and PMOD estimates for MBF at stress, but significantly overestimated MBF at rest [see Fig. 5(b)]. Fermi modeling showed strong correlations against PMOD and Carimas, but it significantly overestimated MBF values, compared to all other modeling applications [Table V, Fig. 5(d)]. These MR-derived MBF overestimations are in agreement with previous studies demonstrating rest [19] and stress-rest overestimations [41] compared with PET estimates. Further work needs to be done to assess which methodological disparities may cause consistent differences in MBF quantification between MR and PET [18], [19], [40]–[43] and to what degree these can affect the diagnostic performance of quantitative MR and PET protocols.

C. Study Limitations

Our diagnostic performance comparison between Carimas and PMOD was performed in a small pilot cohort. However, this is the first study comparing the diagnostic ability of different PET perfusion analysis software for detecting reduced MBF in obstructive CAD, which showed considerable differences between the two techniques. Any changes in the acquisition protocol, the ^{15}O-water dose or the reconstruction technique would necessitate a diagnostic performance reassessment for both MBF quantification techniques [2], [6]. Our MR versus PET analysis was assessed in a small subgroup of patients. For DCE-MRI, we used a single bolus protocol that may be prone to arterial input function saturation effects at the peak of contrast enhancement, which can lead to MBF overestimations [10], [28]. Arterial input function saturation could be more pronounced in our 3T data, compared to perfusion data from 1.5T. Our group previously demonstrated that DP modeling is less dependent on arterial input function saturation compared to Fermi modeling (at 3T) [12]. Fermi modeling may derive smaller systematic bias against PET compared to our findings, if either dual bolus protocols [28] and/or 1.5T [10] would be used for minimizing signal saturation. Despite any Fermi-derived overestimations due to arterial input function saturation effects, our findings are consistent with other studies which showed that Fermi estimates were systematically increased compared to DP modeling (at 3T) [12], to model-independent, two-compartmental and Patlak model analysis (mixture of 1.5 and 3T were used) [44] as well as to uptake model and model-independent analysis (at 1.5T) [10].

V. Conclusion

In conclusion, we demonstrated consistently superior diagnostic performance for the detection of obstructive CAD when PMOD was used versus Carimas in ^{15}O-water PET data. Although we showed strong, significant cross-correlations between MR against PET quantitative perfusion analysis, PMOD and DP analysis detected comparable and higher hemodynamic differences between obstructive versus (no, minor, or non)-obstructive CAD, compared to Carimas and Fermi analysis.

Our MR method assessments against the optimum PET reference standard technique for perfusion analysis showed promising results in per segment level and can support further multimodality assessments in larger patient cohorts. Further MR versus PET assessments may help to determine the comparative diagnostic performance of both quantitative methodologies for obstructive CAD detection.

ACKNOWLEDGMENT

The authors would like to thank Siemens Gmbh for supplying the works in progress software and to the radiographers of the Clinical Research Imaging Centre for their contributions to the image acquisition protocols. The Edinburgh Imaging Facility QMRI and Wellcome Trust Clinical Research Facility (Edinburgh) are supported by the National Health Service Research Scotland. The Centre for Cardiovascular Science is the recipient of a British Heart Foundation Centre of Research Excellence Award under Grant RE/08/001.

REFERENCES

[1] C. Jaarsma *et al.*, "Diagnostic performance of noninvasive myocardial perfusion imaging using single-photon emission computed tomography, cardiac magnetic resonance, and positron emission tomography imaging for the detection of obstructive coronary artery disease," *J. Amer. College Cardiol.*, vol. 59, no. 19, pp. 1719–1728, May 2012.

[2] J. Knuuti, S. Kajander, M. Mäki, and H. Ukkonen, "Quantification of myocardial blood flow will reform the detection of CAD," *J. Nucl. Cardiol.*, vol. 16, no. 4, pp. 497–506, Aug. 2009.

[3] A. R. Patel *et al.*, "Assessment of advanced coronary artery disease: Advantages of quantitative cardiac magnetic resonance perfusion analysis," *J. Amer. College Cardiol.*, vol. 56, no. 7, pp. 561–569, Aug. 2010.

[4] H. J. Harms *et al.*, "Automatic generation of absolute myocardial blood flow images using [^{15}O]H_2O and a clinical PET/CT scanner," *Eur. J. Nucl. Med. Mol. Imag.*, vol. 38, no. 5, pp. 930–939, May 2011.

[5] A. Bol *et al.*, "Direct comparison of [13N]ammonia and [15O]water estimates of perfusion with quantification of regional myocardial blood flow by microspheres," *Circulation*, vol. 87, no. 2, pp. 512–525, Feb. 1993.

[6] H. Iida *et al.*, "Measurement of absolute myocardial blood flow with $H_2{}^{15}O$ and dynamic positron-emission tomography. Strategy for quantification in relation to the partial-volume effect," *Circulation*, vol. 78, no. 1, pp. 104–115, Jul. 1988.

[7] S. V. Nesterov *et al.*, "Myocardial perfusion quantitation with ^{15}O-labelled water PET: High reproducibility of the new cardiac analysis software (Carimas)," *Eur. J. Nucl. Med. Mol. Imag.*, vol. 36, no. 10, pp. 1594–1602, Apr. 2009.

[8] I. Danad *et al.*, "Hybrid imaging using quantitative $H_2{}^{15}O$ PET and CT-based coronary angiography for the detection of coronary artery disease," *J. Nucl. Med.*, vol. 54, no. 1, pp. 55–63, Jan. 2013.

[9] H. J. Harms *et al.*, "Comparison of clinical non-commercial tools for automated quantification of myocardial blood flow using oxygen-15-labelled water PET/CT," *Eur. Heart J. Cardiovasc. Imag.*, vol. 15, no. 4, pp. 431–441, Apr. 2014.

[10] J. D. Biglands *et al.*, "Comparison of the diagnostic performance of four quantitative myocardial perfusion estimation methods used in cardiac MR imaging: CE-MARC substudy," *Radiology*, vol. 275, no. 2, pp. 393–402, May 2015.

[11] A. Huber *et al.*, "Magnetic resonance perfusion of the myocardium: Semiquantitative and quantitative evaluation in comparison with coronary angiography and fractional flow reserve," *Invest. Radiol.*, vol. 47, no. 6, pp. 332–338, Jun. 2012.

[12] G. Papanastasiou *et al.*, "Quantitative assessment of myocardial blood flow in coronary artery disease by cardiovascular magnetic resonance: Comparison of Fermi and distributed parameter modeling against invasive methods," *J. Cardiovasc. Magn. Reson.*, vol. 18, no. 1, pp. 1–13, Sep. 2016.

[13] S. A. Kajander *et al.*, "Clinical value of absolute quantification of myocardial perfusion with (15)O-water in coronary artery disease," *Circulation Cardiovasc. Imag.*, vol. 4, no. 6, pp. 678–684, Nov. 2011.

[14] V. Berti *et al.*, "Segmental quantitative myocardial perfusion with PET for the detection of significant coronary artery disease in patients with stable angina," *Eur. J. Nucl. Med. Mol. Imag.*, vol. 43, no. 8, pp. 1522–1529, Jul. 2016.

[15] M. M. Hajjiri *et al.*, "Comparison of positron emission tomography measurement of adenosine-stimulated absolute myocardial blood flow versus relative myocardial tracer content for physiological assessment of coronary artery stenosis severity and location," *J. Amer. College Cardiol. Imag.*, vol. 2, no. 6, pp. 751–758, Jun. 2009.

[16] D. A. Broadbent *et al.*, "Myocardial blood flow at rest and stress measured with dynamic contrast-enhanced MRI: Comparison of a distributed parameter model with a Fermi function model," *Magn. Reson. Med.*, vol. 70, no. 6, pp. 1591–1597, Dec. 2013.

[17] S. P. Sourbron and D. L. Buckley, "Tracer kinetic modeling in MRI: Estimating perfusion and capillary permeability," *Phys. Med. Biol.*, vol. 57, no. 2, pp. R1–R33, Jan. 2012.

[18] C. A. Miller *et al.*, "Voxel-wise quantification of myocardial blood flow with cardiovascular magnetic resonance: Effect of variations in methodology and validation with positron emission tomography," *J. Cardiovasc. Magn. Reson.*, vol. 16, no. 1, p. 11. Jan. 2014.

[19] G. Morton *et al.*, "Quantification of absolute myocardial perfusion in patients with coronary artery disease: Comparison between cardiovascular magnetic resonance and positron emission tomography," *J. Amer. College Cardiol.*, vol. 60, no. 16, pp. 1546–1555, Oct. 2012.

[20] M. C. Williams *et al.*, "Computed tomography myocardial perfusion vs ^{15}O-water positron emission tomography and fractional flow reserve," *Eur. Radiol.*, vol. 27, no. 3, pp. 1114–1124, Jun. 2016.

[21] D. R. Messroghli, A. Greiser, M. Fröhlich, R. Dietz, and J. Schulz-Menger, "Optimization and validation of a fully-integrated pulse sequence for modified look-locker inversion-recovery (MOLLI) T1 mapping of the heart," *J. Magn. Reson. Imag.*, vol. 26, no. 4, pp. 1081–1086, Oct. 2007.

[22] M. D. Cerqueira *et al.*, "Standardized myocardial segmentation and nomenclature for tomographic imaging of the heart: A statement for healthcare professionals from the cardiac imaging committee of the council on clinical cardiology of the American heart association," *Circulation*, vol. 105, no. 4, pp. 539–542, Jan. 2002.

[23] P. A. L. Tonino *et al.*, "Angiographic versus functional severity of coronary artery stenoses in the FAME study: Fractional flow reserve versus angiography in multivessel evaluation," *J. Amer. College Cardiol.*, vol. 55, no. 25, pp. 2816–2821, Jun. 2010.

[24] I. Adachi *et al.*, "Assessment of myocardial perfusion by dynamic O-15-labeled water PET imaging: Validation of a new fast factor analysis," *J. Nucl. Cardiol.*, vol. 14, no. 5, pp. 698–705, Sep./Oct. 2007.

[25] F. Hermansen *et al.*, "Measurement of myocardial blood flow with oxygen-15 labelled water: Comparison of different administration protocols," *Eur. J. Nucl. Med.*, vol. 25, no. 7, pp. 751–759, Jul. 1998.

[26] G. Blomqvist, "On the construction of functional maps in positron emission tomography," *J. Cerebr. Blood Flow Metab.*, vol. 4, no. 4, pp. 629–632, Dec. 1984.

[27] H. B. W. Larsson *et al.*, "Myocardial perfusion modeling using MRI," *Magn. Reson. Med.*, vol. 35, no. 5, pp. 716–726, May 1996.

[28] G. Papanastasiou *et al.*, "Measurement of myocardial blood flow by magnetic resonance perfusion imaging: Comparison of distributed parameter and Fermi models with single and dual bolus," *J. Cardiovasc. Magn. Reson.*, vol. 17, no. 17, pp. 1–10, Feb. 2015.

[29] M. Jerosch-Herold, N. Wilke, and A. E. Stillman, "Magnetic resonance quantification of the myocardial perfusion reserve with a Fermi function model for constrained deconvolution," *Med. Phys.*, vol. 25, no. 1, pp. 73–84, Jan. 1998.

[30] A. Garpebring, N. Ostlund, and M. Karlsson, "A novel estimation method for physiological parameters in dynamic contrast-enhanced MRI: Application of a distributed parameter model using Fourier-domain calculations," *IEEE Trans. Med. Imag.*, vol. 28, no. 9, pp. 1375–1383, Sep. 2009.

[31] E. R. DeLong, D. M. DeLong, and D. L. Clarke-Pearson, "Comparing the areas under two or more correlated receiver operating characteristic curves: A nonparametric approach," *Biometrics*., vol. 44, no. 3, pp. 837–845, Sep. 1988.

[32] S. V. Nesterov *et al.*, "Quantification of myocardial blood flow in absolute terms using (82)Rb PET imaging: The RUBY-10 study," *JACC Cardiovasc. Imag.*, vol. 7, no. 11, pp. 1119–1127, Nov. 2014.

[33] I. Danad *et al.*, "Quantitative assessment of myocardial perfusion in the detection of significant coronary artery disease: Cutoff values and diagnostic accuracy of quantitative [(15)O]H2O PET imaging," *J. Amer. College Cardiol.*, vol. 64, no. 14, pp. 1464–1475, Oct. 2014.

[34] T. D. Karamitsos *et al.*, "Relationship between regional myocardial oxygenation and perfusion in patients with coronary artery disease: Insights from cardiovascular magnetic resonance and positron emission tomography," *Circulation Cardiovasc. Imag.*, vol. 3, no. 1, pp. 32–40, Jan. 2010.

[35] A. A. Lammertsma, R. De Silva, L. I. Araujo, and T. Jones, "Measurement of regional myocardial blood flow using C15O2 and positron emission tomography: Comparison of tracer models," *Clin. Phys. Physiol. Meas.*, vol. 13, no. 1, pp. 1–20, Jan. 1992.

[36] D. Feng, Z. Wang, and S. C. Huang, "A study on statistically reliable and computationally efficient algorithms for the measurement of local cerebral blood flow with positron emission tomography," *IEEE Trans. Med. Imag.*, vol. 12, no. 2, pp. 182–188, Jun. 1993.

[37] K. Chen *et al.*, "Generalized linear least squares method for fast generation of myocardial blood flow parametric images with N-13 ammonia PET," *IEEE Trans. Med. Imag.*, vol. 17, no. 2, pp. 236–243, Apr. 1998.

[38] J. S. Lee *et al.*, "Generation of parametric image of regional myocardial blood flow using H(2)(15)O dynamic PET and a linear least-squares method," *J. Nucl. Med.*, vol. 46, no. 10, pp. 1687–1695, Jul. 2005.

[39] R. Boellaard, P. Knaapen, A. Rijbroek, G. J. Luurtsema, and A. A. Lammertsma, "Evaluation of basis function and linear least squares methods for generating parametric blood flow images using 15O-water and positron emission tomography," *Mol. Imag. Biol.*, vol. 7, no. 4, pp. 273–285, Jul. 2005.

[40] J. P. Pärkkä *et al.*, "Comparison of MRI and positron emission tomography for measuring myocardial perfusion reserve in healthy humans," *Magn. Reson. Med.*, vol. 55, no. 4, pp. 772–779, Apr. 2006.

[41] N. A. Pack *et al.*, "Estimating myocardial perfusion from dynamic contrast-enhanced CMR with a model-independent deconvolution method," *J. Cardiovasc. Magn. Reson.*, vol. 10, no. 1, pp. 1–15, Nov. 2008.

[42] Y. Tomiyama *et al.*, "Quantification of myocardial blood flow with dynamic perfusion 3.0 Tesla MRI: Validation with (15) O-water PET," *J. Magn. Reson. Imag.*, vol. 42, no. 1, pp. 754–762, Sep. 2015.

[43] T. Fritz-Hansen, J. D. Hove, K. F. Kofoed, H. Kelbaek, and H. B. Larsson, "Quantification of MRI measured myocardial perfusion reserve in healthy humans: A comparison with positron emission tomography," *J. Magn. Reson. Imag.*, vol. 27, no. 4, pp. 818–824, Apr. 2008.

[44] N. A. Pack and E. V. R. DiBella, "Comparison of myocardial perfusion estimates from dynamic contrast-enhanced magnetic resonance imaging with four quantitative analysis methods," *Magn. Reson. Med.*, vol. 64, no. 1, pp. 125–137, Jul. 2010.